

# Exogenous–endogenous surfactant interaction yields heterogeneous spreading in complex branching networks

Richard McNair<sup>1</sup>, Fernando Temprano-Coletto<sup>2</sup>, François J. Peaudecerf<sup>3</sup>, Frédéric Gibou<sup>4</sup>, Paolo Luzzatto-Fegiz<sup>4</sup>, Oliver E. Jensen<sup>1</sup>, Julien R. Landel<sup>1,\*</sup>

<sup>1</sup>Department of Mathematics, University of Manchester, Manchester M13 9PL, UK

<sup>2</sup>Andlinger Center for Energy and the Environment, Princeton University, Princeton, New Jersey 08544, USA

<sup>3</sup>Univ Rennes, CNRS, IPR (Institut de Physique de Rennes) – UMR 6251, F - 35000 Rennes, France

<sup>4</sup>Department of Mechanical Engineering, University of California, Santa Barbara, California 93106, USA

(Dated: November 15, 2023)

Experiments have shown that surfactant introduced to a liquid-filled maze can find the solution path. We reveal how the maze-solving dynamics arise from interactions between the added surfactant and endogenous surfactant present at the liquid surface. We simulate the dynamics using a nonlinear model solved with a discrete mimetic scheme on a graph. Endogenous surfactant transforms local spreading into a non-local problem with an omniscient view of the maze geometry, key to the maze-solving dynamics. Our results offer insight into surfactant-driven transport in complex networks such as lung airways.

Recent experiments [1] showed that surfactant, made visible by dye, can ‘solve’ a liquid maze (Fig. 1(a), Supplementary Movie 1 [2]). The surfactant propagates along the solution path, with little advance into lateral branches. This phenomenon seems counterintuitive, as no mechanism appears to draw the surfactant preferentially to the maze exit: one might expect Marangoni stresses to spread the surfactant throughout the whole maze. Yet, the surfactant proceeds with apparent awareness of the whole geometry. Although no quantitative theory exists, a hypothesis was suggested based on the potential effect of pre-existing, ‘endogenous’ surfactant in the maze liquid [1]. The spread of the ‘exogenous’ (added) surfactant would be influenced by the endogenous surfactant, in a manner sensitive to the maze geometry. Inspired by these observations, we investigate the impact of *endogenous* surfactant on the spreading of *exogenous* surfactant on thin liquid layers confined in asymmetric branching networks.

Whether from natural or contaminant sources, endogenous surfactants are usually undetectable *a priori*, but have macroscopic influence on flow dynamics across numerous applications [3–8]. Natural endogenous surfactant in human lungs can affect exogenous surfactant therapies [9–14] for various diseases, including acute respiratory distress syndrome (ARDS) [15]. Although efficacy of surfactant replacement therapy is indisputable for neonatal respiratory distress syndrome [16–19], there remains debate for other pathologies [20–23], including ARDS, which has a 40% mortality rate in the US [24]. To understand mixed results from clinical trials [20], experimental and theoretical models analysed physical, chemical and biological processes in surfactant transport through branching networks simulating lungs [13, 25, 26]. In distal lung airways, where surfactant therapy is effective, Marangoni transport dominates gravitational transport [11, 13, 27, 28]. Endogenous surfactants can affect therapeutic surfactant transport, preventing it from reaching distal airways [9–12, 14, 29, 30].

Pulmonary surfactant models have used simplifying geometric assumptions to reduce analytical, computational and experimental difficulties. Single-airway models [14, 31]

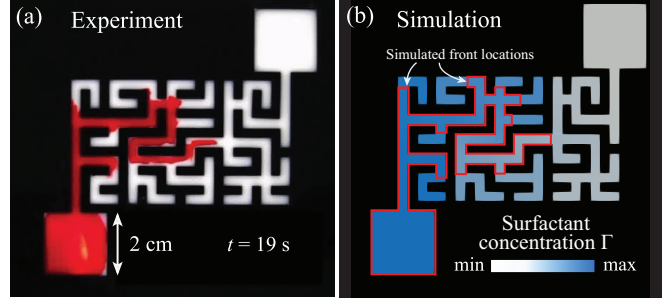


FIG. 1. (a) Photograph of the liquid maze experiment [1]: surfactant deposited at the inlet finds the solution path with minimal penetration into lateral branches, as shown by red dye advected by Marangoni forces. (b) Results from our model (2) showing the concentration (blue-scale) of the surfactant field in the same geometry; the red front is the exogenous–endogenous boundary.

may suppress crucial dynamics associated with branching [12, 32]. More complex models used a Weibel morphometry [33], which yields a dichotomous, symmetric and self-similar branching network [9–12, 27, 34, 35]; however, human lungs are asymmetric and highly irregular [36–38]. Recent models [32, 39], which neglected Marangoni spreading, showed that transport by air flow and gravity in asymmetric lungs can yield heterogeneity in surfactant distribution. The maze experiments of [1] were not designed to model surfactant transport in lungs; nevertheless, the two problems share key underlying physical features. Understanding surfactant dynamics in mazes can give insight about heterogeneities affecting surfactant spreading in large complex networks, such as human lungs.

To test the hypothesis that endogenous surfactant explains the maze-solving behaviour of exogenous surfactant [1], and provide new physical insight, we model surfactant transport on a thin film confined in a 1D branching network, replicating the maze geometry from [1]. The experimental maze consists of a network of grooves in an acrylic substrate, with larger 20 x 20 mm branches at the inlet and outlet (Fig. 1(a)). The large outlet creates an asymmetry in the geometry. Branches were filled with a 50% milk-cream mixture, which provides a

dense, viscous liquid contrasting with red tracer dye added at the inlet. A surfactant drop (0.3% w/w soap–water solution) was deposited at the inlet at  $t = 0$ . Dye is buoyant in the milk, and therefore remains at the surface. Within 60 s, one of the red dye fronts, assumed to follow the exogenous surfactant fronts, reached the outlet, through the solution path of length 155 mm (Sec. S1 [40]).

We assume the dynamics are governed by a balance of viscous and Marangoni stresses, that solubility and diffusion of surfactant are negligible, and that inertia and interface deformation are negligible, as shown quantitatively in [40]. Endogenous and exogenous contributions are modeled as a single surfactant concentration field  $\Gamma$ . The axial and vertical coordinates are  $x$  and  $z$ ,  $t$  is time,  $u|_s$  the surface axial velocity, and  $\gamma$  the surface tension. Variables are normalized by appropriate physical scales [40], such that e.g.  $0 \leq z \leq 1$ . The key equations expressing surfactant conservation and stress balance at the surface are therefore, in nondimensional variables,

$$\Gamma_t + (u|_s \Gamma)_x = 0, \quad \text{and} \quad \gamma_x = u_z|_s, \quad (1a,b)$$

where subscripts in  $x, z, t$  denote partial derivatives, and  $u_z|_s$  is the viscous stress at the surface. To introduce key ideas, ignore initially the effect of lateral ( $y$ ) confinement, such that to leading order the viscous flow in the interior is governed by  $u_{zz} = p_x$ . Integrating twice in  $z$  and assuming that the volume flux along the channel is uniformly zero, such that  $\int_0^1 u dz = 0$ , one finds the surface velocity  $u|_s = p_x/6$  and viscous stress  $u_z|_s = 2p_x/3$ . Eliminating  $p_x$  gives  $u_z|_s = 4u|_s$ . The nondimensional surfactant concentration and surface tension are related by  $\gamma_x = -\Gamma_x$  [40]; substituting this relation, together with  $u_z|_s = 4u|_s$ , into (1b) yields  $u|_s = -\frac{1}{4}\Gamma_x$ . Eliminating  $u|_s$  in (1a) yields an equation that only involves  $\Gamma$ ,

$$\Gamma_t = \frac{1}{4}(\Gamma \Gamma_x)_x \equiv \frac{1}{8}(\Gamma^2)_{xx}. \quad (2)$$

An alternative derivation of (2), starting from lubrication theory, is possible [40]. If we include the effect of lateral no-slip boundaries at  $y = \pm W/2$ , the factor of 1/4 in (2) and  $u|_s$  is replaced by a positive coefficient  $f(W) < 1/4$ , calculated *a priori* as a function of  $W$ . This factor is a nonessential time scaling, as we rescale  $t$  by experimental completion time; however, this analysis shows that narrow channels significantly reduce the surface velocity, helping to keep the flow within the viscous limit (for [1]  $W \approx 0.94$  yielding  $f \approx 0.15$ ).

Model (2) is solved numerically in a branching network simulating the experimental maze topology, illustrated in Fig. 2. At junctions, we impose continuity of surfactant concentration and flux, whilst no flux is imposed at dead-ends (Sec. S2 [40]). The dye fronts are computed by Lagrangian integration of the surface velocity  $u|_s$ . To model the initial conditions, we assume that exogenous surfactant is deposited instantaneously and uniformly at the inlet at  $t = 0$ . The normalised initial concentration is set to  $\Gamma = 1$  at the inlet, whilst the rest of the maze has initial endogenous surfactant concentration  $\Gamma = \delta$  everywhere, where  $0 < \delta < 1$  is an empirical parameter. The branches are numbered as illustrated in

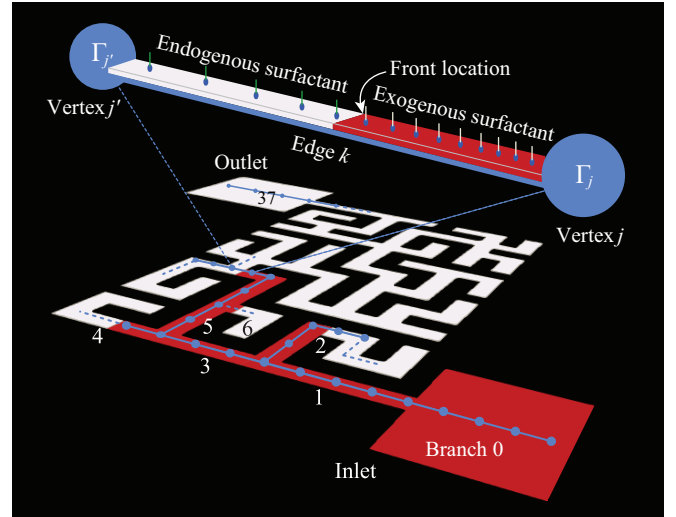


FIG. 2. Schematic showing how the transport model (2) is implemented in a maze mimicking the experiment, with the branch numbering scheme indicated (Fig. S1 [40]). The maze topology is modelled by a 1D branching network (blue). Along each edge, the model results are used to advect the exogenous surfactant fronts (red).

Fig. 2 (see [40] for further details). Branch  $i$  of length  $L_i$  (normalised by the solution path length) has longitudinal coordinate  $0 \leq x_i \leq L_i$ . Internal branches have lengths representative of the experiment. The greater width of the inlet ( $i = 0$ ) and outlet ( $i = 37$ ) branches is treated by constructing 1D equivalents. Since the outlet has small variations in concentration, its length  $L_{37}$  is calculated by dividing its surface area by the width of an interior branch. The inlet length  $L_0$  is calculated by matching the amount of initial exogenous surfactant.

We estimate the ratio of endogenous to exogenous surfactant mass from the equilibrium state of the experiment, as encoded by the ratio of white versus red surface areas (Sec. S2.4 [40]). To avoid numerical instabilities, care is taken to regularize the initial surfactant concentration distribution between the inlet and the first branch (Sec. S2.2 [40]). The time at which the front enters branch 1 is labelled as  $t = 0$ . As noted earlier, in the model, we re-scale time so that the completion time (when the front enters the outlet) matches the experiment up to a multiplying factor  $\tau_{end}$  chosen between  $0.5 \leq \tau_{end} \leq 1.5$ .

To solve the system of equations of the form (2), coupled between each of the branches of the maze, we use a mimetic finite-difference numerical method, which balances fluxes at junctions to machine precision. Mimetic finite-difference methods [41–43] use tools from graph theory and discrete calculus to obtain finite-difference operators which reproduce desired features of vector calculus operators. As shown in Fig. 2, we represent the maze as a graph with vertices at every junction and dead end. Extra vertices are placed along each edge to refine the discretisation. We construct finite-difference mimetic operators on this graph using the incidence matrix of the network  $A$ , the columns of which correspond to the vertices of the graph, and the rows of which correspond to the edges. Each edge is assigned an orientation directed away from the maze inlet. Components of  $A$  are zero except

at vertices where an edge leaves  $(-1)$ , and where an edge enters  $(+1)$ . Metric information is encapsulated by the diagonal edge and vertex length matrices  $L$  and  $V$  respectively. Each component of  $L$  is the length of an edge, and each component of  $V$  is one half the sum of lengths of every edge incident to the corresponding vertex — an important nuance ensuring mass conservation (see Sec. S3.1 [40]). The matrix  $L^{-1}A$  is therefore a finite difference gradient operator acting on scalar functions defined on the graph's vertices, and is second order accurate at edge midpoints. Likewise,  $-V^{-1}A^T$  is a divergence operator acting on functions defined at edge midpoints, and is second order accurate at the vertices. The concentration of surfactant at the vertices of the graph form the components of vector  $\Gamma(t)$ . The system of differential equations of the form (2) solved on the graph is found by combining gradient and divergence operators into a Laplacian, and is therefore

$$\frac{d\Gamma}{dt} = -\frac{f(W)}{2} V^{-1} A^T L^{-1} A \Gamma^2, \quad (3)$$

with  $\Gamma^2$  the component-wise square of  $\Gamma$ . This mimetic finite-difference formulation automatically implements no-flux boundary conditions for all bounding vertices of the graph (dead ends), and continuity of concentration and flux for all junctions within the graph. A semi-implicit scheme solves this system of equations in time (Sec. S3.2 [40]). Simultaneously, we solve the equation tracking the dye fronts, which in branch  $i$  at  $x_i = \Lambda_i(t)$  is  $\partial\Lambda_i/\partial t = u|_s(\Lambda_i, t) = -f(W) \Gamma_x(\Lambda_i, t)$ . When a front reaches a junction, new fronts are created in the downstream branches.

To reduce computational costs and provide additional insight, we consider the limit of small concentration gradients, which arises in applications where concentration differences between exogenous and endogenous surfactants are small. We decompose the concentration into a time- and space-averaged component and a fluctuating component:  $\Gamma = \bar{\Gamma} + \hat{\Gamma}(x, t)$ , with  $|\hat{\Gamma}| \ll \bar{\Gamma}$ . Model (2) simplifies to the linear diffusion equation  $\hat{\Gamma}_t = f(W) \bar{\Gamma} \hat{\Gamma}_{xx}$ . In the discrete mimetic representation, the Laplacian operator  $f(W) \bar{\Gamma} V^{-1} A^T L^{-1} A$  has orthogonal eigenvectors  $\phi_n$  under an inner product  $\langle \phi_l, \cdot \phi_m \rangle = \phi_l^T V \phi_m$  (Sec. S4 [40]). The vector of vertex concentrations can be decomposed in a sum of eigenmodes, namely  $\Gamma(t) = \sum_{n=1}^N A_n \phi_n e^{-\lambda_n t}$ , with amplitudes  $A_n = \langle \phi_n, \Gamma(t=0) \rangle$ ;  $\lambda_n$  are the corresponding eigenvalues. In the linear regime, the concentration in the maze can be approximated without the need for time integration, by instead using only a finite number  $N$  of eigenmodes.

We test our models by comparing their predictions to the dye front locations in the experiments, as shown in Fig. 3(a), which plots time versus location along the global solution path; the inset shows data for a lateral branch. The nonlinear model (shown by the black continuous line) captures the spreading dynamics. Its least-square error relative to the experiment is minimized by setting the order-one coefficients  $\delta = 0.15$  and  $\tau_{\text{end}} = 0.24$  [40]. In the experiments, fronts in lateral branches are observed to eventually recede after initially advancing; this is most visible near the inlet (Supplementary Movie [2]); an example is shown in the inset of

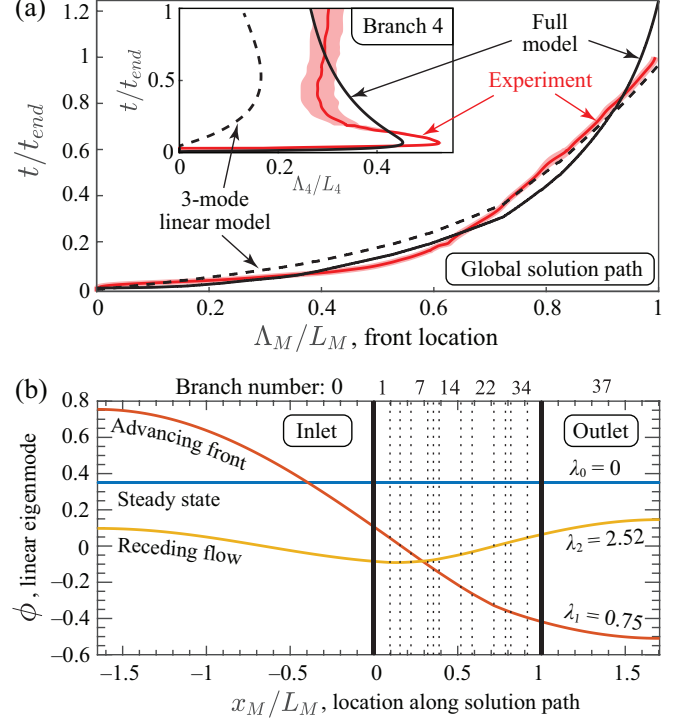


FIG. 3. (a) Front location  $\Lambda_M(t)$  in time along the solution path, normalised by overall length  $L_M$ , from experiments (red curves, experimental error shaded pink), nonlinear model (black curves), and 3-mode linear model (dashed curves). Inset shows lateral branch 4. (b) First 3 eigenmodes of the linear model along the solution path, with eigenvalues  $\lambda$  shown. Thick vertical black lines show the start and end points. Dashed lines show junctions.

Fig. 3(a). This receding effect occurs as the concentration at the beginning of the lateral branch eventually decreases over time, as the exogenous surfactant spreads across the rest of the maze, yielding a reversal of the Marangoni stress. The nonlinear model captures the flow reversal qualitatively, generally overpredicting relaxation time (inset of Fig. 3(a)). The nonlinear model predictions are not sensitive to the exact value of  $\delta$ : any value in the range  $0.02 \leq \delta \leq 0.21$  captures the dynamics in the experiment.

Since the shapes of the eigenmodes depend only on the network geometry, transport dynamics in branching networks can be studied from the dominant eigenmodes and eigenvalues, without having to solve the full nonlinear transport model. The maze-solving dynamics described above are already reproduced by a linear model truncated to just three modes, as shown by the dashed lines in Fig. 3(a). The front location on the global solution path is captured quantitatively. The spatial structure of each mode is in Fig. 3(b). The zeroth mode represents the surfactant concentration at steady state,  $t \rightarrow \infty$ . The first mode,  $\lambda_1 = 0.75$ , has a decreasing profile along the solution path, corresponding to the main concentration gradient driving the front, key to the maze-solving behaviour. The second mode,  $\lambda_2 = 2.52$ , presents a wavy profile, which, in combination with the first mode, controls the receding dynamics observed in lateral branches. The exact temporal evolution requires computation of the mode amplitudes, which depend on

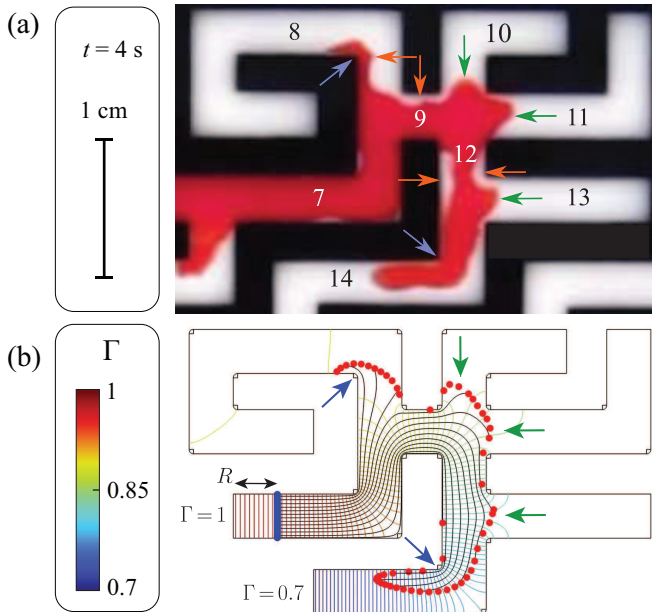


FIG. 4. (a) Experiment, showing branches 7–14. (b) 2D nonlinear simulation. Tracers (red dots) are advected from their starting position (blue dots) along Lagrangian trajectories (black lines). Experimental features are reproduced qualitatively: the front spreads inside sharp corners (blue arrows) and centrally at straight junctions (green arrows), owing to the bending of the concentration contours.

initial conditions. If three modes were used,  $\delta \approx 0.03$  minimized the least-square error. Using a larger number of modes, e.g. of order 100, recovers  $\delta \approx 0.15$  found by the nonlinear model. The main challenge for the linear model is to capture the nonlinear distribution of concentration at  $t = 0$ , better approximated using a larger number of modes.

To assess the importance of 2D dynamics neglected in the model, we perform a 2D simulation of the surfactant transport through branches 7–14 (see Fig. 4). We use COMSOL® to solve the 2D analogue of the 1D model (2), namely  $\Gamma_t = \nabla \cdot (\Gamma \nabla \Gamma)/4$ , in the maze geometry. A good match to experiment is achieved by imposing  $\Gamma = 1$  at the entrance of branch 7 and  $\Gamma = 0.7$  at the exit of branch 14, with initial condition  $\Gamma = 0.7$  everywhere; as before, care is taken to regularize the initial  $\Gamma$  field [40]. We use the particle-tracing module to track the exogenous–endogenous surfactant front. Dominant dynamical features are reproduced by the 2D model (Fig. 4). In the experiments, the exogenous surfactant tends to spread along the inside of sharp corners (blue arrows), whilst it spreads through the middle of the path as it enters new branches from a junction (green arrows). The 2D simulation captures qualitatively these behaviours, which are due to the compression of surfactant concentration level curves at inside corners (Fig. 4(b)). The nonlinear model appears consistent with surfactant dynamics on 2D confined surfaces. However, the 2D simulation does not capture some of the gaps that appear between the maze walls and dye (orange arrows). These features could be due to aspects omitted from the model such as geometrical imperfections, surface deformation at menisci or chemical heterogeneities.

Our model reveals the importance of exogenous–endogenous surfactant interaction in the maze-solving behaviour. Although the model makes assumptions about the endogenous surfactant, our results show that the model is robust; the maze-solving dynamics continue to be reproduced as the ratio of endogenous to exogenous concentration is varied across one order of magnitude. Through the invisible endogenous surfactant, the exogenous surfactant is ‘aware’ of the whole network topology. The large area of the outlet compared to that of the lateral branches ensures that large concentration gradients remain along the solution path, thereby driving the exogenous surfactant to the outlet. In lateral branches, compression of endogenous surfactant limits access by exogenous surfactant. The elliptic nature of the spatial differential operator in (2) means that the surfactant spreads through the maze with an *omniscient* view of the geometry, since together the exogenous and endogenous surfactants fill the whole maze at all times.

Although our model is not designed to simulate surfactant transport in lungs, it may provide insight and novel methodologies for studying surfactant therapies for lungs. Its essential ingredients, endogenous surfactant [9–14] and network asymmetry [36–38], are characteristic of lungs. Exogenous surfactant delivering drugs to the distal airways and alveoli may spread non-uniformly through the lung, reducing drug efficacy. The model could inspire lung-scale models to test the impact of lung network asymmetry on surfactant drug delivery. Our mimetic finite-difference implementation on a network is amenable to scale-up, as we found from preliminary tests on a network with  $O(10^4)$  branches based on real lung scans. If the linear regime applies, the transport model decomposes into a series of modes computed from the network topology, thus helping understand surfactant transport without computationally expensive simulations. Our model framework provides a novel approach compared to single-branch models [9–12, 34, 35], which overlook complex lung topology, and molecular dynamic simulations [44–47], which are numerically expensive to run over a whole lung.

Our model reveals how the combination of asymmetry in the maze network and exogenous–endogenous surfactant interactions are key to understanding confined transport problems in complex branching networks, such as lungs.

J.R.L. and O.E.J. acknowledge financial support from EPSRC grant EP/T030739/1. P.L.-F. acknowledges support from NSF CAREER grant 2048234. F.T.-C. acknowledges support from a Distinguished Postdoctoral Fellowship from the Andlinger Center from Energy and the Environment at Princeton University. For the purpose of Open Access, the authors have applied a Creative Commons Attribution (CC BY) licence to any Author Accepted Manuscript version arising.

\* Corresponding author: julien.landel@manchester.ac.uk

[1] F. Temprano-Coletto, F. J. Peaudecerf, J. R. Landel, F. Gibou, and P. Luzzatto-Fegiz, *Phys. Rev. Fluids* **3**, 100507 (2018).

[2] Supplementary videos at [URL will be inserted by publisher] of our nonlinear simulation show how the surfactant field in the lateral branches compresses and then relaxes at later times, leading to the receding behaviour observed.

[3] F. J. Peaudecerf, J. R. Landel, R. E. Goldstein, and P. Luzzatto-Fegiz, *Proc. Natl. Acad. Sci. USA* **114**, 7254 (2017).

[4] A. Hourlier-Fargette, A. Antkowiak, A. Chateauminois, and S. Neukirch, *Soft Matter* **13**, 3484 (2017).

[5] H. Manikantan and T. M. Squires, *J. Fluid Mech.* **892** (2020).

[6] G. Koleski, A. Vilquin, J.-C. Loudet, T. Bickel, and B. Pouliquen, *Phys. Fluids* **32**, 092108 (2020).

[7] A. Faugaret, Y. Duguet, Y. Fraigneau, and L. Martin Witkowski, *J. Fluid Mech.* **900**, A42 (2020).

[8] F. Temprano-Coletto, S. M. Smith, F. J. Peaudecerf, J. R. Landel, F. Gibou, and P. Luzzatto-Fegiz, *Proc. Natl. Acad. Sci. USA* **120**, 10.1073/pnas.2211092120 (2023).

[9] F. F. Espinosa, A. H. Shapiro, J. J. Fredberg, and R. D. Kamm, *J. Appl. Physiol.* **75**, 2028 (1993).

[10] J. Grotberg, D. Halpern, and O. Jensen, *J. Appl. Physiol.* **78**, 750 (1995).

[11] D. Halpern, O. E. Jensen, and J. B. Grotberg, *J Appl Physiol* **85**, 333 (1998).

[12] Y. L. Zhang, O. K. Matar, and R. V. Craster, *Med. Eng. Phys.* **25**, 115 (2003).

[13] A. Z. Stetten, S. V. Iasella, T. E. Corcoran, S. Garoff, T. M. Przybycien, and R. D. Tilton, *Curr. Op. Colloid Interface Sci.* **36**, 58 (2018).

[14] C. García-Mouton, M. Echaide, L. A. Serrano, G. Orellana, F. Salomone, F. Ricci, B. Pioselli, D. Amidani, A. Cruz, and J. Pérez-Gil, *Pharmaceutics* **15**, 10.3390/pharmaceutics15010256 (2023).

[15] A. Anzueto, R. P. Baughman, K. K. Guntupalli, J. G. Weg, H. P. Wiedemann, A. A. Raventós, F. Lemaire, W. Long, D. S. Zaccardelli, and E. N. Pattishall, *New Eng. J. Med.* **334**, 1417 (1996).

[16] M. J. Avery M. E., *Am. J. Dis. Child.* **97**, 517 (1959).

[17] A. H. Jobe, *New Eng. J. Med.* **328**, 861 (1993).

[18] R. J. Rodriguez, *Respir. Care* **48**, 279 (2003).

[19] H. Halliday, J. Perinat. **28**, S47 (2008).

[20] S. Baudouin, *New England Journal of Medicine* **351**, 853 (2004).

[21] Y. Y. Zuo, R. A. W. Veldhuizen, A. W. Neumann, N. O. Petersen, and F. Possmayer, *Biochimica et Biophysica Acta-Biomembranes* **1778**, 1947 (2008).

[22] M. J. Sankar, N. Gupta, K. Jain, R. Agarwal, and V. K. Paul, J. Perinatol. **36**, S36–S48 (2016).

[23] R. A. W. Veldhuizen, Y. Y. Zuo, N. O. Petersen, J. F. Lewis, and F. Possmayer, *Expert Review of Respiratory Medicine* **15**, 597 (2021).

[24] G. D. Rubenfeld, E. Caldwell, E. Peabody, J. Weaver, D. P. Martin, M. Neff, E. J. Stern, and L. D. Hudson, *New England Journal of Medicine* **353**, 1685 (2005), pMID: 16236739.

[25] R. Levy, D. B. Hill, M. G. Forest, and J. B. Grotberg, *Integrative Comparative Biol.* **54**, 985 (2014).

[26] B. Baer, L. M. P. Souza, A. S. Pimentel, and R. A. Veldhuizen, *Biochem. Pharmacol.* **164**, 64 (2019).

[27] F. F. Espinosa and R. D. Kamm, *J. Appl. Physiol.* **86**, 391 (1999).

[28] J. B. Grotberg, *Ann. Rev. Biomed. Eng.* **3**, 421 (2001).

[29] O. E. Jensen and J. B. Grotberg, *J. Fluid Mech.* **240**, 259 (1992).

[30] J. L. Bull, L. K. Nelson, J. Walsh, J. T. M. R. Glucksberg, S. Schürch, and J. B. Grotberg, *J. Biomech. Eng.* **121**, 89 (1999).

[31] B. Baer, E. J. Veldhuizen, F. Possmayer, C. Yamashita, and R. Veldhuizen, *Discovery Medicine* **26**, 207 (2018).

[32] A. Kazemi, B. Louis, D. Isabey, G. F. Nieman, L. A. Gatto, J. Satalin, S. Baker, J. B. Grotberg, and M. Filoche, *PLOS Comp. Biol.* **15**, 1 (2019).

[33] E. R. Weibel and D. M. Gomez, *Science* **137**, 577 (1962).

[34] M. Filoche, C.-F. Tai, and J. B. Grotberg, *Proc. Natl. Acad. Sci.* **112**, 9287 (2015).

[35] A. Copploe, M. Vatani, C. J. W., and H. Tavana, *Ann. Biomed. Eng.* **47**, 1435 (2019).

[36] K. Horsfield and G. Cumming, *J. Appl. Physiol.* **24**, 373 (1968).

[37] M. Tawhai, P. Hunter, J. Tschirren, J. Reinhardt, G. McLennan, and E. Hoffman, *J. Appl. Physiol.* **97**, 2310 (2004).

[38] A. Schmidt, S. Zidowitz, A. Kriete, T. Denhard, S. Krass, and H. Peitgen, *Computerized Med. Imaging Graphics* **28**, 203 (2004).

[39] S. Elias-Kirma, A. Artzy-Schnirman, H. Sabatan, C. Dabush, D. Waisman, and J. Sznitman, *Journal of biomechanics* **122**, 110458 (2021).

[40] See Supplemental Material at [URL will be inserted by publisher] for further details about the models, their numerical simulation and data analysis.

[41] A. N. Tikhonov and A. A. Samarskii, *USSR Comp. Math. & Math. Phys.* **1**, 5 (1962).

[42] A. van der Schaft, *Systems & Control Lett.* **101**, 21 (2017).

[43] J. M. Hyman and M. Shashkov, *Computers & Math. with Appl.* **33**, 81 (1997).

[44] C. Laing, S. Baoukina, and P. D. Tieleman, *Phys. Chem. Chem. Phys.* **11**, 1916 (2009).

[45] S. Baoukina and P. D. Tieleman, *Biophys. J.* **100**, 1678 (2011).

[46] L. M. P. Souza, J. B. Nascimento, A. L. Romeu, E. D. Estrada-López, and A. S. Pimentel, *Coll. Surf. B: Biointerfaces* **167**, 345 (2018).

[47] L. M. P. Souza, M. C. Lima, L. F. S. Bezerra, and A. S. Pimentel, *Chem. Phys.* **563**, 111704 (2022).